



Full length article

Fabrication of carbon nanotube functionalized MIL-101(Fe) for enhanced visible-light photocatalysis of ciprofloxacin in aqueous solution

Deyi Yan^a, Han Hu^a, Naiyun Gao^b, Jinshao Ye^a, Huase Ou^{a,*}^a Guangdong Key Laboratory of Environmental Pollution and Health, School of Environment, Jinan University, Guangzhou, 510632, China^b State Key Laboratory of Pollution Control and Resources Reuse, College of Environmental Science and Engineering, Tongji University, Shanghai, 200082, China

ARTICLE INFO

Keywords:

Radical oxidation
Metal-organic frameworks
Photocatalysis
Degradation
Antibiotics

ABSTRACT

Improving the performance of metal-organic frameworks (MOFs) through modifications is an important issue to expand their potential applications. In the current study, multi-walled carbon nanotube functionalized MIL-101(Fe) (CNT@MIL-101(Fe)) was synthesized and used to construct a visible-light photocatalysis system for elimination of ciprofloxacin. CNT@MIL-101(Fe) has a lower band gap energy (2.19 eV) than MIL-101(Fe) (2.46 eV), rendering it the visible light absorption from 400 nm to 565 nm. In the CNT@MIL-101(Fe)-photocatalysis system, some optimized reaction conditions were: CNT doping ratio = 5%, pH = 3.0, [H₂O₂] vs. [CNT@MIL-101(Fe)] mass ratio = 11.3. Under 2.0 mW cm⁻² visible light irradiation, degradation of ciprofloxacin followed an apparent pseudo-first-order kinetic reaction rate at 6.85 × 10⁻⁴ s⁻¹. Using CNT@MIL-101(Fe), faster activation and electron transfer were achieved due to the high conductivity of CNT, resulting in a higher removal efficiency of ciprofloxacin (3.02 μM, ~90% at 45 min) than using MIL-101(Fe) (~65%). Furthermore, the iron ions leakage of CNT@MIL-101(Fe) was only half the one of MIL-101(Fe), suggesting a better stability in water. The reactive mechanism was confirmed to be ·OH oxidation, in which visible photocatalysis was the dominant reaction. Generally, CNT@MIL-101(Fe) has enhanced performance and stability, which can act as potential catalyst of organic contaminants.

1. Introduction

Metal-organic frameworks (MOFs) have become one of the most attractive novel classes of materials for scientists and engineers due to their good crystallinity, tunable structure, high porosity and large surface area [1]. Common structures of MOFs contain organic linkers (ligands) and metal-core nodes, which are constructed by covalent bonds. Theoretically, MOFs can have infinite structures. Any metallic element in the periodic table can be selected as alternative metal nodes, while various carboxylic and other organic matters can be applied as linkers for MOF synthesis. These diverse combinations and easily tailored structures result in their extensive potential applications, including catalytic synthesis [2], gas storage/separation [3], biomedical applications [4] and heterogeneous photocatalysis [5].

Photocatalysis represents an attractive potential to not only remedy polluted waters, but also utilize harness solar energy [6–9]. Recently, increasing researches have attempted to use MOFs for photocatalysis degradation of organic contaminants in aqueous mediums [10–12]. Among various MOFs, Fe-MOFs could be one practicable class photocatalyst. Advantages of Fe-MOFs includes environment-safety, cost-

effective and photoresponsive feature. The most familiar Fe-based MOFs are the MIL series (MIL-101, MIL-100 and MIL-53, etc.) [13]. Under light irradiation, an excitation of electrons from HOMO (oxygen and/or nitrogen orbitals) to LUMO (metal cluster) occurs, followed by the electron transport from the MOF interface to donors (such as H₂O₂). These processes generate highly reactive radicals species (such as hydroxyl radicals ·OH), which degrade and even mineralize organic contaminants in water [14]. Therefore, Fe-based MOFs have the potential to act as photocatalysts for water treatment.

However, MOFs (also for Fe-based MOFs) exhibit a few weak points that impede their full potential as photocatalysts in water treatment. The poor stability, especially for some MOFs with low valence metal cores, could be the most critical issue [15]. It was reported that significant decomposition of some MOFs, including Zn-DMOF-1, Zn-UMCM-1, Cu-BTC (HKUST-1) and MOF-5 series, occurred even under moist air [16,17], not to mention in water. Furthermore, the large dimension and semiconductor feature render pristine MOFs the low efficient solar light harvesting, charge separation and transportation capacity, which were not conducive to photocatalytic reactions [18]. To mitigate these drawbacks, several strategies have been developed. One

* Corresponding author.

E-mail address: touhuase@jnu.edu.cn (H. Ou).<https://doi.org/10.1016/j.apsusc.2019.143836>

Received 21 July 2019; Received in revised form 15 August 2019; Accepted 29 August 2019

Available online 30 August 2019

0169-4332/ © 2019 Published by Elsevier B.V.

approach is selecting combinations with strong chemical-bands to form steady MOFs [19]. For example, high valence metals, including Ti, Zr, Fe, Al and Cr, were selected to form core nodes, as well as strong organic acids to form the ligands. Based on Pearson's hard/soft acid/base principle, these strong acid-basic combinations will be more stable in acid and neutral aqueous conditions [20]. Another approach is modifying MOFs with some substrates, such as semiconductor nanoparticles [21], carbon nanotubes (CNT) [22], graphene oxide (GO) [23], etc. Addition of these substrates may improve the performance of MOFs. For example, semiconductor nanoparticles can enhance the separation of electrons and holes. GO can improve the dispersion and firmness of MOFs in water, while CNT addition may provide a better electrons transportation performance.

To date, only a few researches have synthesized CNT functionalized MOFs for photocatalysis [22,24]. For Fe-based MOFs, the detailed information about the performance improvement as photocatalyst after doping CNT is still unclear. In this study, CNT functionalized MIL-101(Fe) (named CNT@MIL-101(Fe)) was fabricated and characterized. A typical antibiotic, ciprofloxacin (CIP), was selected as the target, while a visible light photocatalysis system using CNT@MIL-101(Fe) and H₂O₂ was developed and optimized for CIP degradation. Comparison of the degradation efficiency and stability between CNT@MIL-101(Fe) and its parent MIL-101(Fe) was conducted. The reaction mechanism was investigated using electron paramagnetic resonance (EPR). This study can provide useful information for the specific application of CNT@Fe-based MOFs as photocatalysts in aquatic mediums.

2. Materials and methods

2.1. Chemical materials

Multi-walled carbon nanotube (MWCNT, > 98%) was obtained from Chengdu Organic Chemicals CO. LTD., Chinese Academy of Sciences. Its outer diameter is 10–20 nm, and its length is 0.5–2.0 μm. CIP (98%, HPLC grade), benzene-1,4-dicarboxylic acid (H₂BDC, HPLC grade), *N,N*-dimethylformamide (DMF) and 2,2,6,6-tetramethylpiperidine (TEMPO, 98%), 5,5-dimethyl-1-pyrroline *N*-oxide (DPNO, 99%) were obtained from TCI. Analytical grade H₂O₂ (30%) and FeCl₃·6H₂O (98%) were purchased from Sinopharm. Ultrapure water with 18.2 MΩ was used to prepare solutions.

2.2. Synthesis and characterization of CNT@MOFs

MIL-101(Fe) was fabricated using a similar hydrothermal reaction [25]. The typical synthesis procedure was: 2.026 g FeCl₃·6H₂O (7.5 mmol), 0.622 g (3.75 mmol) H₂BDC and 45 mL of DMF were mixed and undergone ultrasonic treatment (15 min). This DMF mixture was transferred to a steel autoclave. After heating at 120 °C (24 h), the product was washed by DMF and 60 °C EtOH until the raw stuff was removed. A drying (70 °C, 30 min) and an activation (150 °C, 10 h) procedures were conducted subsequently.

For CNT@MIL-101(Fe) synthesis, a similar process was performed with some modifications. Typically, different amount (2, 5, 10, 15, 20 wt%) MWCNT was added into 9 mL EtOH, and this suspension was undergone ultrasonic treatment (10 min) to disperse the MWCNT. Subsequently, this suspension was mixed with H₂BDC and FeCl₃·6H₂O in DMF together. After a 5 min ultrasonication, this mixture was transferred to a steel autoclave. After heating at 120 °C (24 h), the following purification processes were similar to MIL-101(Fe).

Characterization of MOFs included the following parameters. A scanning electron microscope (EVO18, Zeiss) was applied to obtain the high-resolution scanning electron microscope (HRSEM) of MOFs. A iS50 infrared spectrometer (Thermo) was applied to measure the Fourier transformed infrared (FT-IR). A UV-3600+ spectrophotometer (Shimadzu) was used to determine 200–850 nm ultraviolet-visible spectrum. A D2 Phaser X-ray diffraction device (Bruker) was employed

to characterize the XRD feature, while a ThermoFisher K-Alpha instrument was used to record X-ray photoelectron spectroscopy (XPS). The specific surface areas of MOFs were measured by the Brunauer–Emmett–Teller (BET).

2.3. Photocatalysis degradation experiments

An irradiation device equipped with light-emitting diodes (white light LEDs, 360–830 nm) was assembled, which was constituted by a replaceable light source, supporting framework and reactor vessel. Irradiation < 400 nm was cut by a 400 nm filter, thus, only visible light was utilized in photocatalysis experiments. The total irradiation intensity was determined to be 2.0 mW cm⁻² on the top of reaction solution, which was measured by an illuminometer. The supporting framework was fabricated using 3D-print, while the reactor vessel contained a series of customized Petri dish.

At first, pH of CIP solution ([CIP]₀ at 3.02 μM) was maintained using H₃PO₄, NaOH and KH₂PO₄ mixed buffered solution. In each group, 20 mL solution in the reactor vessel was shaken orbitally (60 rpm) under particular temperatures (288–308 K). After adding given amount of MOFs, a 60-min pre-absorption was conducted. Photocatalysis experiments were started by adding given amount of H₂O₂ solution (30%) and lighting up the LEDs. At each pre-set time point, 1.0 mL sample was collected, and then was mixed with equivalent sodium sulfite solution to quench potential radicals. The mixture was filtrated by polyethersulfone filter, and then stored in brown amber tubes.

2.4. Quantitative and qualitative analysis of organic pollutant

Quantitative analysis of CIP was carried out by a TripleQuad 5500 HPLC/MS² (AB-Sci). Qualitative analysis of transformation products was conducted by a TOF 6600+ high resolution mass spectrometry (AB-Sci). The determined products were defined to be tentative candidates [26]. Other determination procedures are shown in supplementary materials. A systematic intermediate screening procedure is discussed in our previous study [27].

2.5. Recyclability/stability experiments

In recyclability experiments, the main procedure was similar to the basic photocatalysis degradation experiment (Section 2.3). After the first reaction cycle, the used MOFs powder was separated by centrifugation. The mud was purified with 300 mL deionized water. The slurry was dried at 50 °C (12 h), and then the powder was weighted and used for the next cycle. In stability experiments, the total iron ion (ferric and ferrous) concentrations were determined by an inductive coupled plasma emission spectrometer. XRD and FT-IR were measured following similar methods (Section 2.2).

2.6. Influence factor and mechanism exploration experiments

Four influence factors, including CNT ratio, pH, temperature, [H₂O₂] vs [GO@IL-101(Fe)] mass ratio, were tested by changing the particular factor based on the basic experiment in Section 2.2. EPR was used to determine reactive radicals. DPNO was used as the spin-trapping agent for ·OH. EPR instrument parameters were: power at 11.52 mW; modulation amplitude at 1.00 G; time constant at 78.94 ms; sweep width at 120 G; conversion time at 40 ms; resolution in X at 1024; resolution in Y at 20–45; sweep time at 39.46 s. TEMPO was applied as the radical standard in the quantitative analysis. The spin adduct concentrations were determined using a reported method [28].

2.7. Degradation using actual water matrix

Actual water matrix was obtained from a wastewater treatment plant (WWTP) in Guangzhou City, China. The main treatment processes

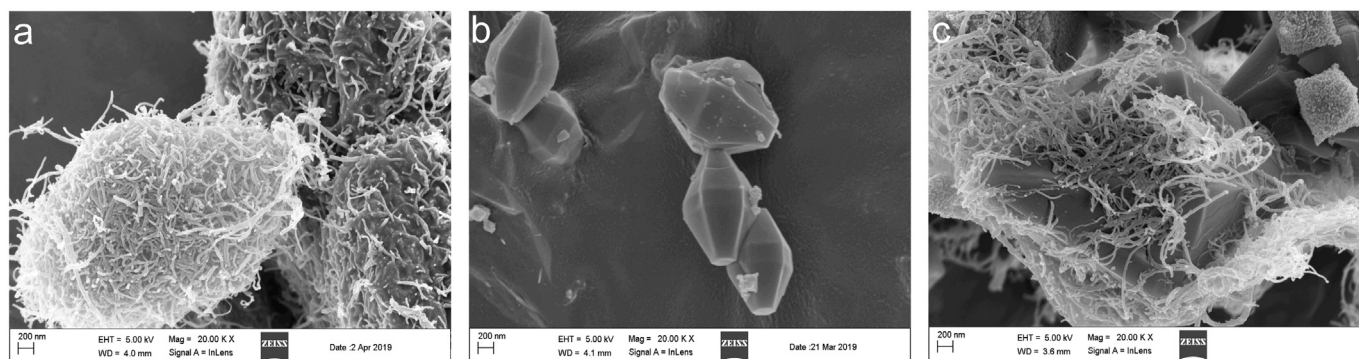


Fig. 1. HRSEM of MWCNT (a), MIL-101(Fe) (b) and CNT@MIL-101(Fe) (c).

of this WWTP included pre-sedimentation, activated sludge biological treatment (anaerobic-anoxic-oxic process), second sedimentation and disinfection (chlorine + ultraviolet). The source water and final effluent were obtained, and the analysis procedure of water parameters is presented in Text S2. Degradation experiment was conducted by adding pre-determined amounts of CIP and CNT@MIL-101(Fe) into the actual water matrix, and the main experimental procedure was similar to Section 2.3.

3. Results and discussion

3.1. Characterization

Fig. 1 shows the HRSEM images of CNT, MIL-101(Fe) and CNT@MIL-101(Fe). CNTs are dense tubes stacked together by dispersive forces (Fig. 1a). MIL-101(Fe) consists of 1.0–2.0 μm regular polyhedron (Fig. 1b). The morphology of CNT@MIL-101(Fe) presents a hybrid feature, as the CNT winding on the MIL-101(Fe) crystal (Fig. 1c). Furthermore, the hybrid CNT@MIL-101(Fe) presents an increasing size than MIL-101(Fe) due to the attachment and reinforcement of CNT. Similar phenomenon was also reported in a previous study [22]. The BET specific surface area were measured. Pure MWCNT had a higher BET ($132.846 \text{ m}^2 \text{ g}^{-1}$) than MIL-101(Fe) ($101.650 \text{ m}^2 \text{ g}^{-1}$). After the modification with MWCNT, the BET specific surface area of CNT@MIL-101(Fe) increased. This increasing BET could improve the adsorption capacity of MOFs.

The FT-IR spectroscopy of CNT showed no evident characteristic peak (Fig. 2a), while MIL-101(Fe) presented a distinct FT-IR pattern with peaks at 750, 1020, 1396, 1583 and 1680 cm^{-1} . Peak 750 cm^{-1} indicated the C–H bond in benzene. Peaks 1396 cm^{-1} and 1583 cm^{-1} suggested the existence of carboxyl (–COO–). Peak 1680 cm^{-1} originated from C=O bonds in carboxyl. These peaks indicated the existence of ligand dicarboxylate linker in MIL-101(Fe). After adding CNT, no evident shifting of characteristic peak was observed. However, the intensity of FT-IR peaks decreased gradually when CNT doping ratio increased. This may be due to the shielding effect induced by CNT around MIL-101(Fe).

Fig. 1b shows the XRD spectrums of MIL-101(Fe) and CNT@MIL-101(Fe). MIL-101(Fe) have four characteristic peaks at $2\theta = 8.5^\circ, 9.6^\circ, 19.5^\circ$ and 21.5° , while CNT@MIL-101(Fe) containing different ratio CNT demonstrated similar patterns, indicating that the addition of CNT did not impede the generation of the MIL-101 crystals. However, the intensities of these peaks gradually decreased when the CNT doping ratio increased, which may be due to the partial distortion of the MIL-101(Fe) framework and the winding of CNT.

The addition of CNT may change the absorption spectrum of MIL-101(Fe), which was measured using Ultraviolet-visible diffuse-reflectance spectrum (UV-Vis DRS, Fig. 2c). For CNT, only a weak reflectance was presented in 200–900 nm. In the contrary, MIL-101(Fe) had a significant light reflectance in the range of 550–900 nm. After

adding CNT, the reflectance ratio in these range gradually decreased, suggesting a potential enhancement of visible light absorption. To evaluate the photo utilization capacity, band gap energy (E_g) was calculated based on a reported method [29]. MIL-101(Fe) has an E_g at 2.46 eV (Fig. 2d), indicating that light irradiation $< 520 \text{ nm}$ can be absorbed and valence electrons can be converted into conduction electrons. For CNT@MIL-101(Fe), E_g was determined to be around 2.19 eV ($\sim 565 \text{ nm}$), indicating an expansion of upper absorption wavelength limit. Considering that natural water bodies contained various natural organic matter and anions, which have significant shielding to UV irradiation but not visible light, this expansion would be benefit to improve the utilization efficiency of visible light for CNT@MIL-101(Fe) photocatalysis system in actual water treatment.

The XPS of CNT@MIL-101(Fe) are presented in Fig. 2. In the survey spectrum of CNT@MIL-101(Fe), peaks representing C, O and Fe elements were observed (Fig. 2e). As shown in Fig. 2f, the C1s peak can be divided into three peaks at 284.9 eV, 285.8 eV and 288.8 eV, which represented the carbon atoms bond (C–C) and carbon organic linkers (C–O and O–C=O) of CNT@MIL-101(Fe). The O1s peak can be deconvoluted into three peaks at 531.2, 531.9 and 533.2 eV, which related to the oxygen atoms in the Fe–O bonds, C–O linkers and C=O linkers, respectively (Fig. 2g). For the Fe2p spectrum, four peaks were observed (Fig. 2h). Among them, peaks at 711.6 eV and 724.8 eV were the characteristic peaks of Fe2p_{3/2} and Fe2p_{1/2}, respectively, proving the existence of F–O bonds in CNT@MIL-101(Fe). These characterizations, including SEM, FT-IR, XRD, XPS, as well as UV-Vis DRS, indicated that the successful syntheses of MIL-101(Fe) and CNT@MIL-101(Fe), and the performance of the later one as photocatalyst may be improved.

3.2. Basic performance and kinetics

To prove the enhanced performances of CNT@MIL-101(Fe), several control experiments were performed. First, adsorption, H₂O₂ oxidation and sole light irradiation were considered. MIL-101(Fe) adsorbed 19% CIP (initial concentration at 3.02 μM) with an equilibrium within 60 min. For 5% CNT@MIL-101(Fe), this value was 21%, which may be due to the slight increasing BET. Thus, a 60 min pre-adsorption was performed in all the subsequent experiments. Sole H₂O₂ oxidation and sole light irradiation had little degradation of CIP. For visible light/H₂O₂ experiment, since visible light cannot activate the splitting of H₂O₂, no CIP degradation was observed. Similar phenomenon was observed in the light/CNT system without radical generation. Light/MIL-101(Fe) and light/CNT@MIL-101(Fe) seemed to have slight degradation of CIP. After 120-min reaction, only 6% and 9% CIP was removed in these two systems. Although short wave visible light can activate these two MOFs to excitation states, the low irradiation intensity (2.0 mW cm^{-2}) and low quantum yield in MOFs [18] limited the degradation efficiency.

CNT/H₂O₂, MIL-101(Fe)/H₂O₂ and CNT@MIL-101(Fe)/H₂O₂ were

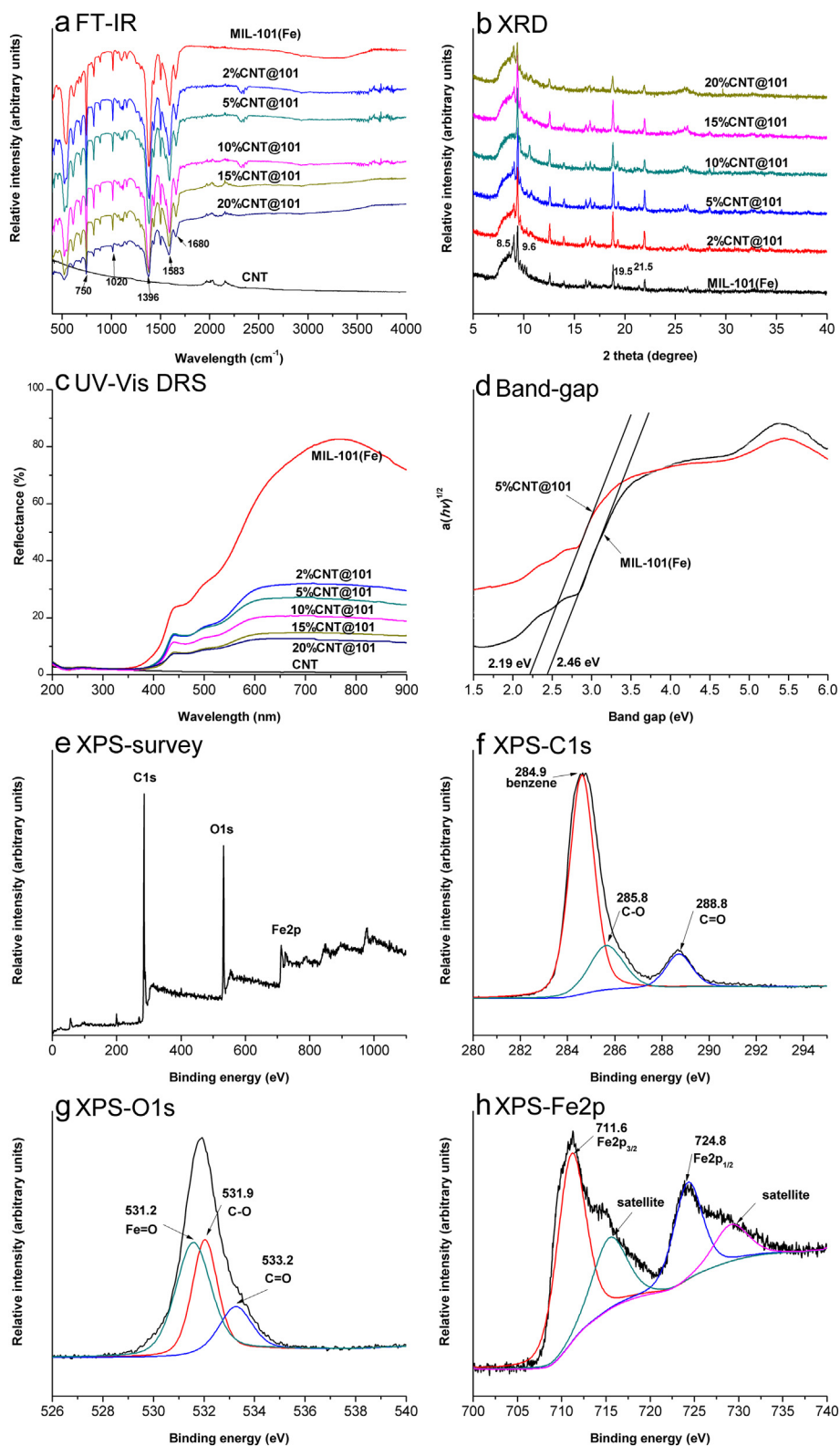


Fig. 2. Characterization of MOFs. (a) FT-IR, (b) XRD, (c) UV-Vis DRS, (d) band-gap, (e) XPS-survey, (f) XPS-C1s, (g) XPS-O1s, (h) XPS-Fe2p.

evaluated (Fig. 3a). No degradation was observed in the CNT/H₂O₂ system. For MIL-101(Fe)/H₂O₂, ~28% CIP was removed by MIL-101(Fe)/H₂O₂ after 120-min reaction, while CNT@MIL-101(Fe)/H₂O₂ presented a lower removal efficiency at ~16%, indicating that both MOFs may induce a Fenton-like reaction. Light/CNT/H₂O₂ was tested, and a negligible removal was observed, suggesting that no

photocatalysis occurred.

Higher removal efficiencies were observed in light/MIL-101(Fe)/H₂O₂ and light/CNT@MIL-101(Fe)/H₂O₂ systems (CNT doping ratio 5%, Fig. 3a). CIP degradation in the light/MIL-101(Fe)/H₂O₂ system presented an S-shape curve (Fig. 3a), which presented an initial slow stage, following by a rapid stage. A slow degradation was observed in

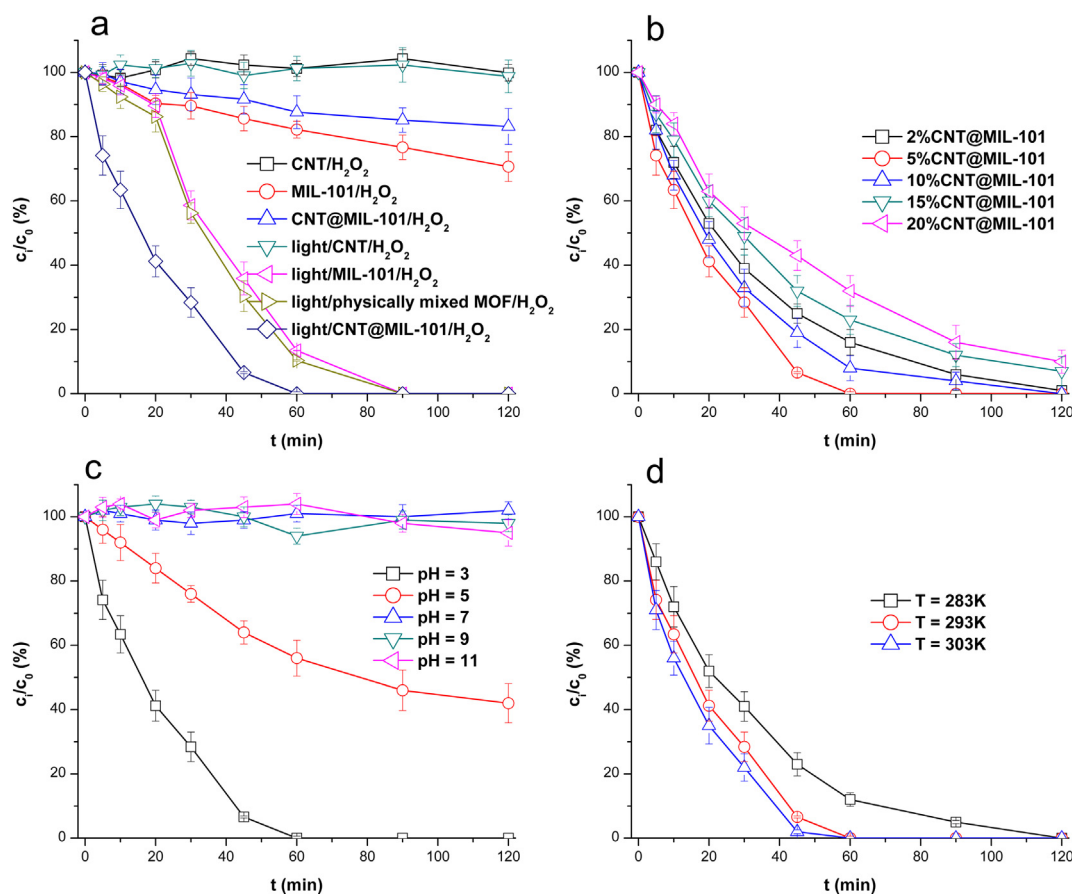


Fig. 3. Removal efficiencies of CIP in CNT@MIL-101(Fe) photocatalysis reactions. (a) basic performance, (b) effect of CNT doping ratio, (c) effect of pH, (d) effects of temperature. Common experimental conditions: irradiation intensity = 2.0 mW cm^{-2} , $[\text{H}_2\text{O}_2]_0 = 165 \text{ mM}$, $[\text{CIP}]_0 = 3.02 \text{ }\mu\text{M}$, $[\text{CNT@MIL-101(Fe)}]_m = 0.5 \text{ g L}^{-1}$, temperature = 298 K, CNT doping ratio = 5%. All the experiments were carried out in triplicate with error bars representing the standard error of the mean.

the former stage ($\sim 30 \text{ min}$), which was reported in previous researches [30,31]. This stage was defined as the induction period, which can be attributed to surface activation of catalysts [32]. Another study supposed that adsorption of reactants on catalysts happened in this stage [31]. On the other hand, the later stage demonstrated a rapid degradation, which may be a radical oxidation stage. Furthermore, physically mixed CNT-MIL-101(Fe) was also prepared with CNT doping ratio at 5%. The removal efficiency of CIP in this light/physically mixed MOF/ H_2O_2 system demonstrated similar pattern compared to the light/MIL-101(Fe)/ H_2O_2 system, implying that physical mixture had little improvement on the MIL-101(Fe) performance.

For light/CNT@MIL-101(Fe)/ H_2O_2 system, there is no induction period. Thus, its degradation efficiency was higher during the early stage. For instance, the CIP removal reached 58% and 90% with CNT@MIL-101(Fe) at 20 min and 45 min, while the ones were 10% and 65% with MIL-101(Fe). After fitting calculation, the degradation of CIP in the light/CNT@MIL-101(Fe)/ H_2O_2 system presented a pseudo-first-order kinetic curve. In the control system (light intensity = 2.0 mW cm^{-2} , $[\text{H}_2\text{O}_2]_0 = 165 \text{ mM}$, temperature = 298 K, $[\text{CIP}]_0 = 3.02 \text{ }\mu\text{M}$, $[\text{CNT@MIL-101(Fe)}]_m = 0.5 \text{ g L}^{-1}$, CNT doping ratio = 5%, pH = 3.0), the apparent rate constants k_{obs} reached $6.85 \times 10^{-4} \text{ s}^{-1}$ (Table 1). The enhanced performance of CNT@MIL-101(Fe) may be due to the fast generation and separation of charge carriers (electrons and holes) induced by CNT. When visible light is absorbed and activates the sites on CNT@MIL-101(Fe), electrons start to transfer from HOMO (oxygen and/or nitrogen orbitals) to LUMO (metal cluster), and then CNT acts as the electrons transport highway, inducing an efficient separation of photogenerated electrons and holes. Finally, a high efficient catalysis of H_2O_2 into $\cdot\text{OH}$ is achieved for CIP

Table 1

Apparent kinetic constant k_{obs} in light/CNT@MIL-101(Fe)/ H_2O_2 systems.

Systems	$k_{\text{obs}} (\times 10^{-4} \text{ s}^{-1})$
pH = 3.0 (control)	6.85
pH = 5.0	1.65
CNT doping ratio = 2%	5.07
CNT doping ratio = 5% (control)	6.85
CNT doping ratio = 10%	6.10
CNT doping ratio = 15%	3.98
CNT doping ratio = 20%	3.63
T = 288 K	5.03
T = 298 K (control)	6.85
T = 308 K	8.22

Control experiment condition: irradiation intensity = 2.0 mW cm^{-2} , $[\text{H}_2\text{O}_2]_0 = 165 \text{ mM}$, $[\text{CIP}]_0 = 3.02 \text{ }\mu\text{M}$, $[\text{CNT@MIL-101(Fe)}]_m = 0.5 \text{ g L}^{-1}$, temperature = 298 K, CNT doping ratio = 5%, pH = 3.0.

degradation. Of note, the k_{obs} in the current study was close to those reported in the literatures using other photocatalysts. For UV/ TiO_2 , apparent rate constants k_{obs} in the range of $0.80\text{--}7.50 \times 10^{-4} \text{ s}^{-1}$ were reported for CIP degradation (254 nm, total irradiation power: 8 W, TiO_2 concentration: 25–200 mg L^{-1}) [33]. In another study using 500 mg L^{-1} P25 TiO_2 , the k_{obs} was confirmed to be $3.67 \times 10^{-4} \text{ s}^{-1}$ [34]. Considering that normal TiO_2 can only be activated by ultraviolet, whereas CNT@MIL-101(Fe) can utilize visible light, the light/CNT@MIL-101(Fe)/ H_2O_2 system would be a promising method for CIP removal in water.

3.3. Effects of CNT doping ratio, pH, temperature and reactant ratio

CNT doping ratio may have effects on the photocatalysis performance of CNT@MIL-101(Fe). The degradation efficiency increased and reached a peak value with doping ratio at 5% (Fig. 3b). CNT doping can enhance separation of the photogenerated electron-hole pairs and the electron transformation efficiency. Approximate 100% CIP was degraded in the 5% CNT@MIL-101(Fe) photocatalysis system at 60 min. However, as the CNT doping ratio increased (from 5% to 20%), excessive CNT addition can bind outside the MOF, reducing its light absorption surface. Thus, a decline of degradation efficiency was observed (Fig. 3b). In the subsequent experiments, 5% CNT@MIL-101(Fe) was applied.

Effects of pH value, temperature and reactant ratio were tested. Variation of initial pH value had a significant influence (Fig. 3c). Under strong acid condition (pH = 3.00), the fastest degradation rate was achieved. As pH increased (pH = 5.00), the degradation efficiency decreased but still presented a similar kinetics pattern. Under neutral and alkaline conditions, the degradation of CIP can be negligible. Effect of pH can be attributed to the status variations of CNT@MIL-101(Fe) and H₂O₂. The abundant H⁺ in the acid reaction system resulted in the protonation and positive charging of CNT@MIL-101(Fe). Surface protonation attracted more H₂O₂ to achieve a faster reaction. To the contrary, under the alkaline condition, protonation of CNT@MIL-101(Fe) weakened. H₂O₂ can react with OH⁻ to produce hydroperoxyl ions (HO₂⁻, Eq. (1)), reducing the available H₂O₂ [35]. Furthermore, OH⁻ can attach onto Fe(III) clusters, decreasing the activated sites of CNT@MIL-101(Fe). Therefore, acid condition is favorable for the light/CNT@MIL-101(Fe)/H₂O₂ system, and pH = 3.0 was applied in the subsequent experiments.



Temperature of reaction solution would be another influencing factor. As the temperature increased from 283 K to 303 K, degradation efficiency increased slightly (Fig. 3d). High temperature can accelerate the reactant transmission and electron transfer. However, the effect of temperature seemed to be limit under ambient temperature (283 K to 303 K, Table 1). The ratio of [H₂O₂]_m vs. [CNT@MIL-101(Fe)]_m also affected the reaction. The ratio at 11.3 was the optimal. Raising the H₂O₂ concentration can provide more oxidant donors to generate ·OH. On the other hand, the recombination of ·OH aggravated when excessive H₂O₂ was added, which reduced the available ·OH. Similar phenomenon was also observed in other study using UV/H₂O₂ [36].

3.4. Recyclability and stability

Recyclability and stability are important for the MOFs application in water treatment. A three times repetitive experiment was conducted (Fig. 4a). Approximate 100% CIP was removed within 60 min in the first cycle, while it reduced to 96% and 90% in subsequent two cycles, indicating a slight inactivation of CNT@MIL-101(Fe). Leakage of iron ion (Fe³⁺ and Fe²⁺) was measured for the evaluation of CNT@MIL-101(Fe) decomposition (Fig. 4b). During one reaction cycle (120 min reaction) of CNT@MIL-101(Fe) in deionized water (pH = 3.0), ~0.21 mg L⁻¹ iron ion was released, contributing ~0.04% to the total additional mass. For MIL-101(Fe), up to 0.59 mg L⁻¹ iron ion was detected under the same condition. Of note, this slight iron ion leakage would induce a weak Fenton-like reaction in the presence of H₂O₂, which may be the reason for the slight degradation of CIP in MIL-101(Fe)/H₂O₂ and CNT@MIL-101(Fe)/H₂O₂ systems (Fig. 3a). The FT-IR and XRD before and after the three-times repetitive experiment are presented in Fig. 4c–f. For CNT@MIL-101(Fe), FT-IR and XRD patterns and characteristic peaks were preserved, while the characteristic peak intensity of MIL-101(Fe) decreased evidently. All these results indicated that CNT@MIL-101(Fe) is more steady than MIL-101(Fe) for the photocatalysis application in aqueous medium.

3.5. Degradation mechanism

To confirm the dominant reaction mechanism in CNT@MIL-101(Fe) photocatalysis, EPR was applied for the determination of radicals using DPNO as the trapping agent. Only ·OH was detected in the light/CNT@MIL-101(Fe)/H₂O₂ system (Fig. 5a). The intensity variation of ·OH is shown in Fig. 5b. For MIL-101(Fe)/H₂O₂ and CNT@MIL-101(Fe)/H₂O₂ systems, only slow increases were observed, suggesting a weak Fenton-like reaction in the presences of Fe²⁺ and H₂O₂. This is consistent with the concentration variation of iron ion (Fig. 4b) and the slight degradation of CIP in these two systems (Fig. 3a). For light/MIL-101(Fe)/H₂O₂ system, the generation of ·OH followed a slow-fast pattern, which was also consistent with the degradation pattern of CIP (Fig. 3a). This also verified the slow induction period in the initial stage was lack of radicals, while the later rapid degradation stage was attributed to ·OH oxidation. Of note, the intensity of ·OH increased rapidly within 30 min in the light/CNT@MIL-101(Fe)/H₂O₂ system, suggesting a significant acceleration of ·OH generation after CNT doping, which increased the electron separation and transport in hybrid CNT@MIL-101(Fe).

The dominant reactive radical in light/CNT@MIL-101(Fe)/H₂O₂ system was confirmed to be ·OH. Based on the above results, ·OH can be generated through two pathways. First, the Fenton reaction contributed a minor part (Fig. 3a). Second, the light induced photocatalysis was the pre-dominant one. The detailed mechanism involved: visible light irradiation (400–565 nm) induced the excitation of electrons from HOMO (oxygen orbitals in ligands) to LUMO (Fe(II)/Fe(III)), followed by the electron transport between the MOF interface and H₂O₂. Cleavage of H₂O₂ generated reactive ·OH for the degradation of CIP. CNT wrapping enhanced this photocatalysis process.

3.6. Degradation products and pathways

The degradation pathway of CIP can be speculated to be ·OH oxidation. Products identification procedure included molecular weight and MS² fragment comparison. After this procedure, five products were identified (Fig. 6). The extracted ion chromatograms (EICs) and MS² chromatograms (fragment data) are obtained. The predominant transformation mechanism may include cleavage, hydroxylation and carbonylation of CIP induced by ·OH. Product A may be the hydroxyl substituted product of CIP at site 1. ·OH can also attack the piperazine ring, resulting in product B. On the other hand, cleavage on piperazine ring generated product C. The elimination of a H₂O molecule may occur on sites 13 and 14 of product C and remain a double bond, resulting in product D. Furthermore, ·OH would attack site 6 to generate product E. These degradation products and pathways further proved the ·OH oxidation reaction.

3.7. Performance in actual wastewater

Degradation of CIP was tested using actual WWTP water as background matrixes. The basic water quality parameters were determined, and the degradation efficiencies of CIP are presented in Fig. 7. The initial pH value of ultrapure water was 5.80, and it reduced to 3.71 after adding 0.5 g L⁻¹ CNT@MIL-101(Fe). Thus, a reasonable removal efficiency was achieved using ultrapure water without pH adjustment, yet, it was still lower than the one under pH = 3.0. For the WWTP source water and effluent, after adding CNT@MIL-101(Fe), their pH reduced from 7.54 to 7.12 and from 6.97 to 6.31, respectively, which may be due to their intrinsic buffering effect. Unsurprisingly, no removal of CIP was observed in these two water matrixes due to the high pH conditions. In another three reaction groups, pH was adjusted and maintained at ~3.0 using buffer solution. High removal efficiencies of CIP with similar patterns were observed in these three groups, suggesting that the impurities in WWTP actual matrixes had little effect on the performance of CNT@MIL-101(Fe) photocatalysis. These results also confirmed that the light/CNT@MIL-101(Fe)/H₂O₂ system was

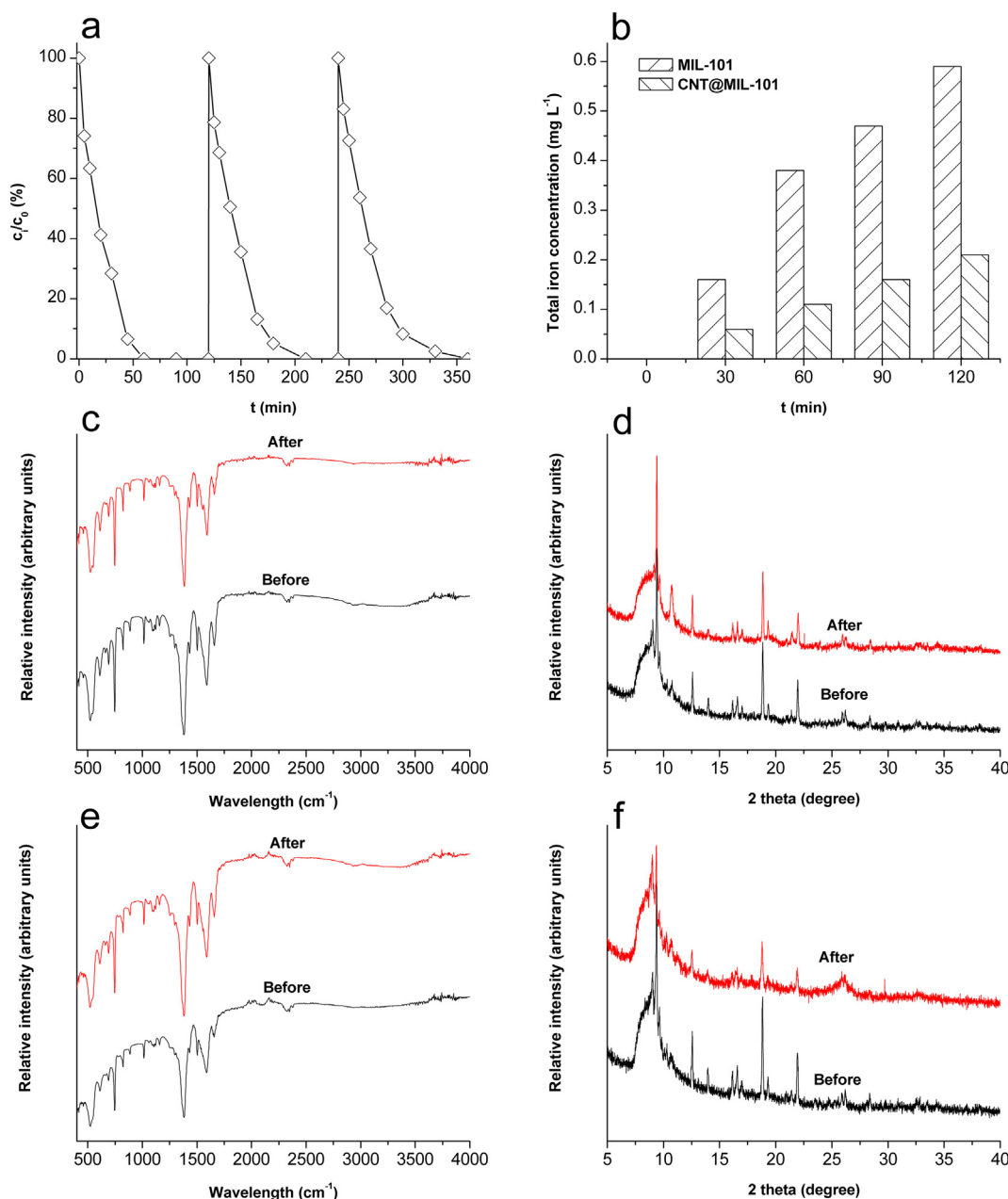


Fig. 4. Recyclability and stability of MOFs. (a) recyclability experiment, (b) iron ion concentration, (c) FT-IR of CNT@MIL-101(Fe) before and after recyclability reaction, (d) XRD of CNT@MIL-101(Fe) before and after recyclability reaction. (e) FT-IR of MIL-101(Fe) before and after recyclability reaction. (f) XRD of MIL-101(Fe) before and after recyclability reaction. Common experimental conditions: irradiation intensity = 2.0 mW cm⁻², [H₂O₂]₀ = 165 mM, [CIP]₀ = 3.02 μM, [CNT@MIL-101(Fe)]_m = 0.5 g L⁻¹, temperature = 298 K, CNT doping ratio = 5%.

susceptive to the pH of aqueous mediums.

4. Conclusions

Synthesized CNT@MIL-101(Fe) has a lower band gap energy (2.19 eV) than its parent MIL-101(Fe), resulting in an expansion of visible light absorption from 520 nm to 565 nm. Under given reaction conditions (2.0 mW cm⁻², pH = 3.0, [H₂O₂]₀ = 165 mM, [CIP]₀ = 3.02 μM, [CNT@MIL-101(Fe)]_m = 0.5 g L⁻¹, CNT doping ratio = 5%), degradation of CIP in the light/CNT@MIL-101(Fe)/H₂O₂ photocatalysis system followed a pseudo-first-order kinetic pattern with a k_{obs} at 6.85 × 10⁻⁴ s⁻¹. The light/CNT@MIL-101(Fe)/H₂O₂ system had a higher CIP removal efficiency (90% at 45 min) than the light/MIL-101(Fe)/H₂O₂ system (65%), which may be due to the fast generation and separation of charge carriers (electrons and holes) induced

by CNT. The reactive mechanism in the light/CNT@MIL-101(Fe)/H₂O₂ system was confirmed to be ·OH oxidation, in which visible photocatalysis was the dominant contributor and Fenton reaction was the minor one. Furthermore, CNT@MIL-101(Fe) presented a better stability than MIL-101(Fe) in aqueous medium. Generally, hybrid CNT@MIL-101(Fe) has an enhanced performance to be a potential photocatalyst for water treatment.

Acknowledgements

This project is supported by the National Natural Science Foundation of China (Grant No. 51778270) and the Fundamental Research Funds for the Central Universities (Grant No. 21617448).

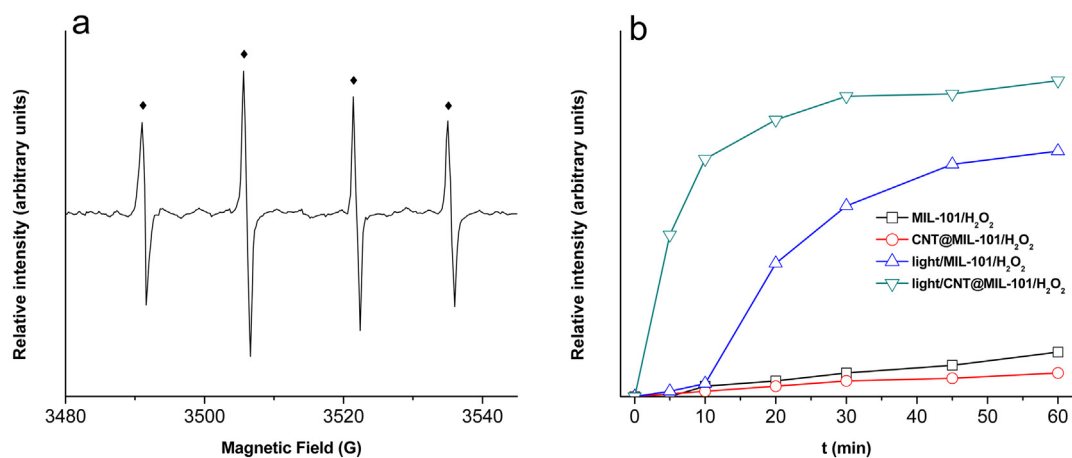


Fig. 5. Degradation mechanism. (a) EPR, (b) relative intensity variation of $\cdot\text{OH}$.

Appendix A. Supplementary data

Detailed descriptions of methods, supporting figures and tables. Contents: Quantitative analysis of CIP and qualitative analysis of

intermediate products (Text S1), Actual water matrix sampling and analysis (Text S2), Operational parameters of mass spectrum (Table S1), BET data (Table S2), Basic water parameters of ultrapure water and actual water matrixes (Table S3), Multiple wavelength LED irradiation

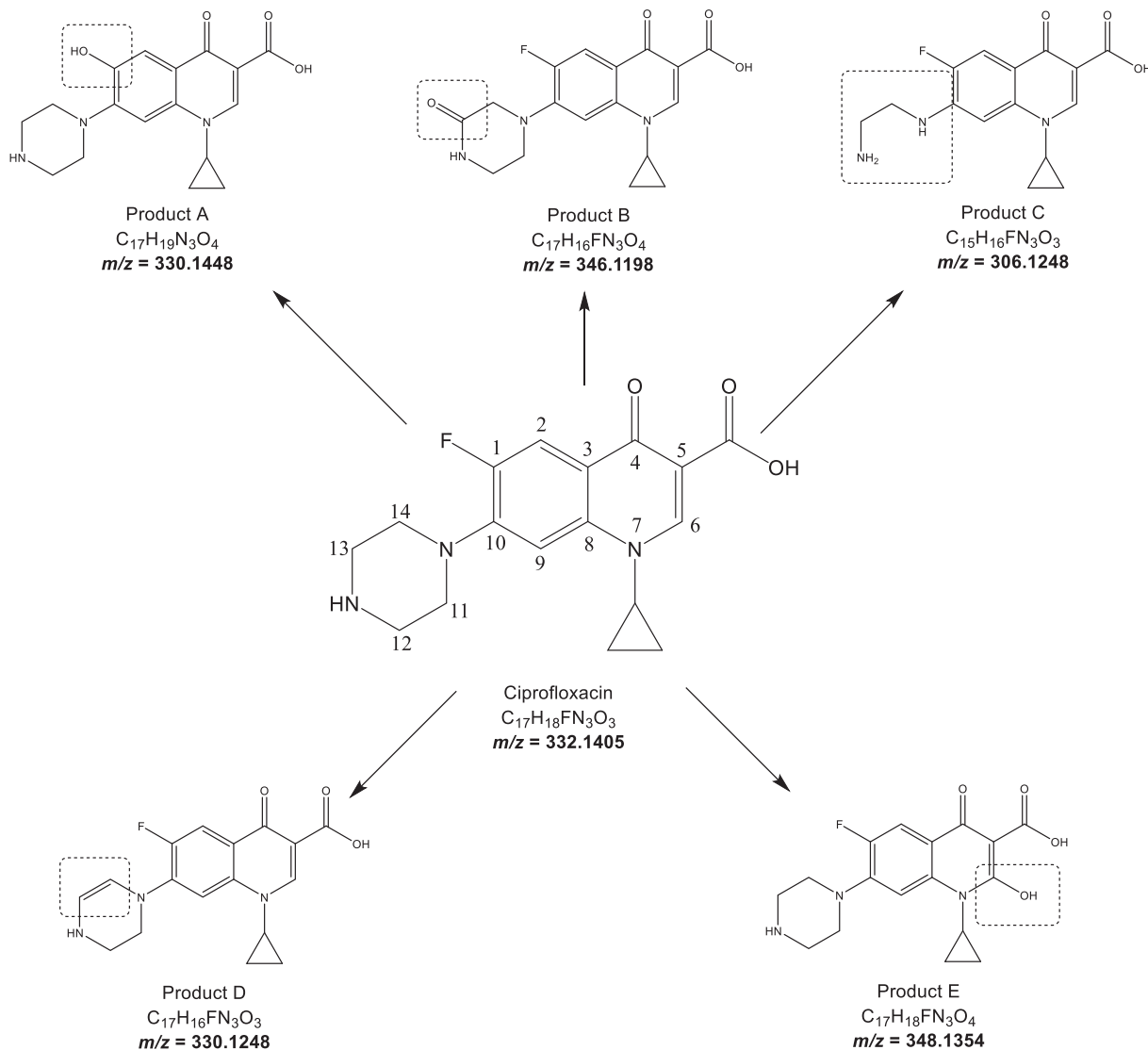


Fig. 6. Proposed generation pathways of CIP degradation products.

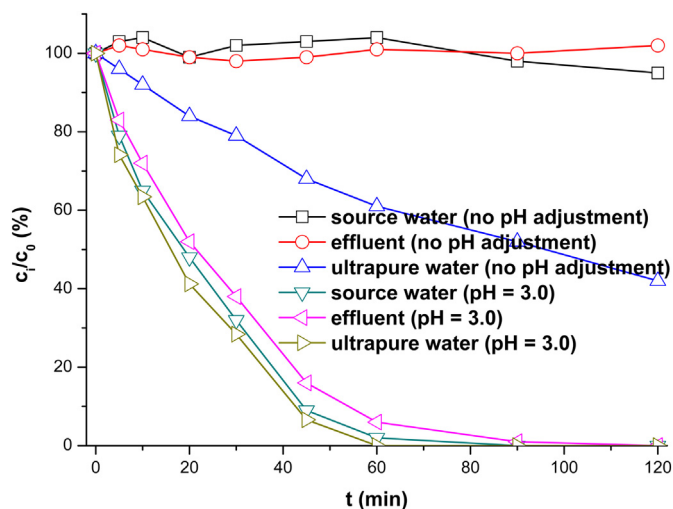


Fig. 7. Removal efficiencies of CIP in actual water matrices. Common experimental conditions: irradiation intensity = 2.0 mW cm^{-2} , $[\text{H}_2\text{O}_2]_0 = 165 \text{ mM}$, $[\text{CIP}]_0 = 3.02 \mu\text{M}$, $[\text{CNT@MIL-101(Fe)}]_m = 0.5 \text{ g L}^{-1}$, temperature = 298 K , CNT doping ratio = 5%.

module (Fig. S1), Control experiments-1 (Fig. S2), Control experiments-2 (Fig. S3), Effect of $[\text{H}_2\text{O}_2]_m$ vs. $[\text{CNT@MIL-101(Fe)}]_m$ (Fig. S4), Extracted ion spectra of observed products (Fig. S5), MS₂ spectrum of observed products (Fig. S6). Supplementary data to this article can be found online at <https://doi.org/10.1016/j.apsusc.2019.143836>.

References

- H. Furukawa, K.E. Cordova, M. O'Keeffe, O.M. Yaghi, The chemistry and applications of metal-organic frameworks, *Science* 341 (2013) 974–985.
- K. Shen, X.D. Chen, J.Y. Chen, Y.W. Li, Development of MOF-derived carbon-based nanomaterials for efficient catalysis, *ACS Catal.* 6 (2016) 5887–5903.
- D. Alezi, Y. Belmabkhout, M. Suyetin, P.M. Bhatt, L.J. Weselinski, V. Solovyeva, K. Adil, I. Spanopoulos, P.N. Trikalitis, A.H. Emwas, M. Eddaoudi, MOF crystal chemistry paving the way to gas storage needs: aluminum-based soc-MOF for CH₄, O₂, and CO₂ storage, *J. Am. Chem. Soc.* 137 (2015) 13308–13318.
- M. Gimenez-Marques, T. Hidalgo, C. Serre, P. Horcajada, Nanostructured metal-organic frameworks and their bio-related applications, *Coordin Chem Rev* 307 (2016) 342–360.
- S.B. Wang, X.C. Wang, Multifunctional metal-organic frameworks for photocatalysis, *Small* 11 (2015) 3097–3112.
- H. Wang, Y. Wu, M. Feng, W. Tu, T. Xiao, T. Xiong, H. Ang, X. Yuan, J.W. Chew, Visible-light-driven removal of tetracycline antibiotics and reclamation of hydrogen energy from natural water matrices and wastewater by polymeric carbon nitride foam, *Water Res.* 144 (2018) 215–225.
- H. Yu, L. Jiang, H. Wang, B. Huang, X. Yuan, J. Huang, J. Zhang, G. Zeng, Modulation of Bi₂MoO₆-based materials for photocatalytic water splitting and environmental application: a critical review, *Small* 15 (2019) 1901008.
- J. Zhang, H. Wang, X. Yuan, G. Zeng, W. Tu, S. Wang, Tailored indium sulfide-based materials for solar-energy conversion and utilization, *J Photochem Photobiol C: Photochem Rev* 38 (2019) 1–26.
- Q. Xia, H. Wang, B. Huang, X. Yuan, J. Zhang, J. Zhang, L. Jiang, T. Xiong, G. Zeng, State-of-the-art advances and challenges of Iron-based metal organic frameworks from attractive features, synthesis to multifunctional applications, *Small* 15 (2019) 1803088.
- J.J. Zhu, P.Z. Li, W.H. Guo, Y.L. Zhao, R.Q. Zou, Titanium-based metal-organic frameworks for photocatalytic applications, *Coordin Chem Rev* 359 (2018) 80–101.
- G. Paille, M. Gomez-Mingot, C. Roch-Marchal, B. Lassalle-Kaiser, P. Mialane, M. Fontecave, C. Mellot-Draznieks, A. Dolbecq, A fully noble metal-free photo-system based on cobalt-polyoxometalates immobilized in a porphyrinic metal-organic framework for water oxidation, *J. Am. Chem. Soc.* 140 (2018) 3613–3618.
- M. Altaf, M. Sohail, M. Mansha, N. Iqbal, M. Sher, A. Fazal, N. Ullah, A.A. Isab, Synthesis, characterization, and photoelectrochemical catalytic studies of a water-stable zinc-based metal-organic framework, *Chemsuschem* 11 (2018) 542–546.
- M. Cheng, C. Lai, Y. Liu, G.M. Zeng, D.L. Huang, C. Zhang, L. Qin, L. Hu, C.Y. Zhou, W.P. Xiong, Metal-organic frameworks for highly efficient heterogeneous Fenton-like catalysis, *Coordin Chem Rev* 368 (2018) 80–92.
- J. Liang, Z.B. Liang, R.Q. Zou, Y.L. Zhao, Heterogeneous catalysis in zeolites, mesoporous silica, and metal-organic frameworks, *Adv. Mater.* 29 (2017) 1701139.
- C. Petit, B. Levasseur, B. Mendoza, T.J. Bandosz, Reactive adsorption of acidic gases on MOF/graphite oxide composites, *Micropor Mesopor Mat* 154 (2012) 107–112.
- P.M. Schoenecker, C.G. Carson, H. Jasuja, C.J.J. Flemming, K.S. Walton, Effect of water adsorption on retention of structure and surface area of metal-organic frameworks, *Ind. Eng. Chem. Res.* 51 (2012) 6513–6519.
- S.S. Kaye, A. Dailly, O.M. Yaghi, J.R. Long, Impact of preparation and handling on the hydrogen storage properties of Zn₄O(1,4-benzenedicarboxylate)₃ (MOF-5), *J. Am. Chem. Soc.* 129 (2007) 14176–14177.
- J.R. Ran, J. Zhang, J.G. Yu, M. Jaroniec, S.Z. Qiao, Earth-abundant cocatalysts for semiconductor-based photocatalytic water splitting, *Chem. Soc. Rev.* 43 (2014) 7787–7812.
- J. Canivet, A. Fateeva, Y.M. Guo, B. Coasne, D. Farrusseng, Water adsorption in MOFs: fundamentals and applications, *Chem. Soc. Rev.* 43 (2014) 5594–5617.
- M.B. Feng, P. Zhang, H.C. Zhou, V.K. Sharma, Water-stable metal-organic frameworks for aqueous removal of heavy metals and radionuclides: a review, *Chemosphere* 209 (2018) 783–800.
- F. Ke, L.H. Wang, J.F. Zhu, Facile fabrication of CdS-metal-organic framework nanocomposites with enhanced visible-light photocatalytic activity for organic transformation, *Nano Res.* 8 (2015) 1834–1846.
- W.P. Xiong, Z.T. Zeng, X. Li, G.M. Zeng, R. Xiao, Z.H. Yang, Y.Y. Zhou, C. Zhang, M. Cheng, L. Hu, C.Y. Zhou, L. Qin, R. Xu, Y.R. Zhang, Multi-walled carbon nanotube/amino-functionalized MIL-53(Fe) composites: remarkable adsorptive removal of antibiotics from aqueous solutions, *Chemosphere* 210 (2018) 1061–1069.
- Y. Zheng, F.C. Chu, B. Zhang, J. Yan, Y.L. Chen, Ultrahigh adsorption capacities of carbon tetrachloride on MIL-101 and MIL-101/graphene oxide composites, *Micropor Mesopor Mat* 263 (2018) 71–76.
- H. Zhang, S. Chen, H.G. Zhang, X.F. Fan, C. Gao, H.T. Yu, X. Quan, Carbon nanotubes-incorporated MIL-88B-Fe as highly efficient Fenton-like catalyst for degradation of organic pollutants, *Front Env Sci Eng* 13 (2019) 18.
- H. Hu, H.X. Zhang, Y. Chen, Y.J. Chen, L. Zhuang, H.S. Ou, Enhanced photocatalysis degradation of organophosphorus flame retardant using MIL-101(Fe)/persulfate: effect of irradiation wavelength and real water matrices, *Chem. Eng. J.* 368 (2019) 273–284.
- E.L. Schymanski, J. Jeon, R. Gulde, K. Fenner, M. Ruff, H.P. Singer, J. Hollender, Identifying small molecules via high resolution mass spectrometry: communicating confidence, *Environ Sci Technol* 48 (2014) 2097–2098.
- H.S. Ou, J. Liu, J.S. Ye, L.L. Wang, N.Y. Gao, J. Ke, Degradation of tris(2-chloroethyl) phosphate by ultraviolet-persulfate: kinetics, pathway and intermediate impact on proteome of *Escherichia coli*, *Chem. Eng. J.* 308 (2017) 386–395.
- Z.S. Wei, F.A. Villamena, L.K. Weavers, Kinetics and mechanism of ultrasonic activation of persulfate: an in situ EPR spin trapping study, *Environ Sci Technol* 51 (2017) 3410–3417.
- R. Lopez, R. Gomez, Band-gap energy estimation from diffuse reflectance measurements on sol-gel and commercial TiO₂: a comparative study, *J Sol-Gel Sci Technol* 61 (2012) 1–7.
- J.G. Carriazo, E. Guelou, J. Barrault, J.M. Tatibouet, S. Moreno, Catalytic wet peroxide oxidation of phenol over Al-cu or Al-Fe modified clays, *Appl. Clay Sci.* 22 (2003) 303–308.
- M.L. Luo, D. Bowden, P. Brimblecombe, Catalytic property of Fe-Al pillared clay for Fenton oxidation of phenol by H₂O₂, *Appl Catal B-Environ* 85 (2009) 201–206.
- C. Park, R.T.K. Baker, Modifications in the catalytic properties of nickel supported on different dielectric oxides, *Chem. Mater.* 14 (2002) 273–280.
- W.A.L. Venancio, C. Rodrigues-Silva, M.G. Maniero, J.R. Guimaraes, Photocatalytic removal of fluoroquinolones and their antimicrobial activity from water matrices at trace levels: a comparison of commercial TiO₂ catalysts, *Water Sci. Technol.* 78 (2018) 1668–1678.
- W.H. Li, C.S. Guo, S. Su, J. Xu, Photodegradation of four fluoroquinolone compounds by titanium dioxide under simulated solar light irradiation, *J Chem Technol Biot* 87 (2012) 643–650.
- G. Boczkaj, A. Fernandes, Wastewater treatment by means of advanced oxidation processes at basic pH conditions: a review, *Chem. Eng. J.* 320 (2017) 608–633.
- J.S. Ye, J. Liu, H.S. Ou, L.L. Wang, Degradation of ciprofloxacin by 280 nm ultraviolet-activated persulfate: degradation pathway and intermediate impact on proteome of *Escherichia coli*, *Chemosphere* 165 (2016) 311–319.